Eidgenössische Technische Hochschule Zürich

Ecole polytechnique fédérale de Zurich
Politecnico federale di Zurigo
Swiss Federal Institute of Technology Zurich

Reconstructing acoustic obstacles by planar and cylindrical waves

J. Li, H. Liu*, H. Sun† and J. Zou‡

Research Report No. 2010-43
December 2010

Seminar für Angewandte Mathematik
Eidgenössische Technische Hochschule
CH-8092 Zürich
Switzerland

*Department of Mathematics, University of California, Irvine, CA 92697, USA. The work of this author is partly supported by NSF grant DMS 0724808.

†Institute of Mathematics, Academy of Mathematics and Systems Science, Chinese Academy of Sciences, Beijing 100190, P. R. China

‡Department of Mathematics, The Chinese University of Hong Kong, Shatin, Hong Kong. The work of the third author was substantially supported by Hong Kong RGC grants (Projects 405110 and 404407).

Reconstructing Acoustic Obstacles by Planar and Cylindrical Waves

Jingzhi Li[*], Hongyu Liu[†], Hongpeng Sun[‡], Jun Zou[§]

Abstract

Following the spirit of the linear sampling method due to Colton and Kirsch, we develop a novel method of reconstructing acoustic obstacles in $\mathbb{R}^2$. There are two major new ingredients in our study. First, the reconstruction scheme makes use of the near-field measurements encoded into the boundary Dirichlet-to-Neumann (DtN) map or the Neumann-to-Dirichlet (NtD) map. Second, both the plane waves and cylindrical waves are shown to meet the reconstruction purpose. Numerical experiments are provided to illustrate the effectiveness of the proposed reconstruction scheme.

1 Introduction

This work is concerned with the inverse problem of imaging obstacles located in the homogeneous space by acoustic wave measurements. Consider an impenetrable scatterer D, which is assumed to be the open complement of an unbounded domain of C^2 class in $\mathbb{R}^2$. The scatterer is allowed to have more than one (but finitely many) obstacle component. The time-harmonic wave propagation in $\mathbb{R}^2\backslash\bar{D}$ is governed by the celebrated Helmholtz equation

$$(\Delta + k^2)u = 0 \quad \text{in} \quad \mathbb{R}^2\backslash\bar{D}, \tag{1.1}$$

where u represents the pressure of the wave. On the boundary ∂D of the obstacle, the wave exhibits various behaviors depending on the physical properties of the underlying obstacle. We have $u = 0$ on ∂D for a *sound-soft* D, $\partial u/\partial\nu = 0$ on ∂D for a *sound-hard* D, and $\partial u/\partial\nu + i\lambda u = 0$ on ∂D for a scatterer D of *impedance type*. Here ν is the exterior unit normal to ∂D and $\lambda \in C^1(\partial D)$ is a positive function. We shall write

$$\mathcal{B}(u) = 0 \quad \text{on} \quad \partial D \tag{1.2}$$

[*]SAM, D-MATH, ETH Zürich, CH-8092 Switzerland. (jingzhi.li@sam.math.ethz.ch)

[†]Department of Mathematics, University of California, Irvine, CA 92697, USA. The work of this author is partly supported by NSF grant DMS 0724808. (hongyul1@uci.edu)

[‡]Institute of Mathematics, Academy of Mathematics and Systems Science, Chinese Academy of Sciences, Beijing 100190, P. R. China. (hpsun@amss.ac.cn)

[§]Department of Mathematics, The Chinese University of Hong Kong, Shatin, Hong Kong. The work of the third author was substantially supported by Hong Kong RGC grants (Projects 405110 and 404407). (zou@math.cuhk.edu.hk)

to denote either of the aforementioned three boundary conditions or of mixed type. We would like to stress that the reconstruction method developed in the present paper is independent of the specific boundary condition. However, for the ease of exposition we stick mostly to Dirichlet or Neumann boundary conditions in our subsequent discussions.

In non-invasive probing, one intends to determine the target obstacle D by the knowledge of the waves away from the object. This inverse problem forms the basis of many areas of science and technology; see e.g. [12, 23, 24] and the references therein. There are two types of wave measurements that were widely employed and investigated in the literature for this inverse problem: the scattering measurement encoded into the far-field pattern, and the boundary measurement encoded into the DtN or NtD map. Correspondingly, many reconstruction schemes have been developed in different settings, among which we would like to mention two: the linear sampling method originated from Colton and Kirsch (see, e.g., [11]) and the enclosure method due to Ikehata (see, e.g., [20–22]). These two schemes have received significant attention in the last decade due to their qualitative aspects. Particularly, these methods require no *a priori* knowledge of the underlying target obstacles. This is of essential importance from a practical viewpoint. There are many developments along this line; see, e.g. [2, 3, 7, 10, 13, 14, 17, 19, 24, 25, 28–30] and the references therein.

In this paper, we are mainly interested in using the boundary measurements for the reconstruction of unknown obstacles, since we have more choices on the probing waves other than planar waves. To that end, we let Ω be an artificial domain containing D. It is assumed that the origin belongs to Ω, and Ω is star-shaped with respect to the origin and of C^2 class. For the convenience of our subsequent study, we let $\partial\Omega$ be parametrically represented by $\partial\Omega := r(d)d$ with $d \in \mathbb{S}^1$ and $\mathbb{S}^1$ being the unit circle in $\mathbb{R}^2$. For the Helmholtz equation (1.1)–(1.2) confined over $\Omega\backslash\bar{D}$, we impose the following boundary condition on the exterior boundary

$$u = f \in H^{1/2}(\partial\Omega) \quad \text{on} \quad \partial\Omega. \tag{1.3}$$

It is assumed that 0 is not an eigenvalue to the problem (1.1)–(1.3. Hence, we have a well-defined Dirichlet-to-Neumann map Λ_D defined as

$$\Lambda_D(f) = \frac{\partial u}{\partial \nu}\bigg|_{\partial\Omega}, \tag{1.4}$$

where $u \in H^1(\Omega\backslash\bar{D})$ is the unique solution to (1.1)–(1.3) and ν denotes the exterior unit normal to $\partial\Omega$. The method we shall develop is to reconstruct D from the knowledge of Λ_D. The crucial ingredient is to introduce the following first kind integral equation

$$\int_{\partial\Omega} (\Lambda_D - \Lambda_0) u(x; d) g(d) ds(d) = \frac{\partial G(x, z)}{\partial \nu(x)}, \tag{1.5}$$

where $u(x; d)$ is a class of solutions to the Helmholtz equation (1.1) depending on a parameter $d \in \mathbb{S}^1$, Λ_0 denotes the DtN map without the inclusion D, and $G(x, z)$ is a Green's function for the Helmholtz equation in Ω with a vanishing Dirichlet boundary

value on $\partial\Omega$. We shall show that $g(d)$ will exhibit different behaviors depending on whether z belongs to the interior or exterior of D. Therefore, we could make use of g as an indicator function to identify D. The idea of using an indicator function over the unit sphere to identify an obstacle was first proposed in [11]. As we mentioned earlier, there are a lot of developments along this line, but mostly based on far-field measurements corresponding to planar incident waves. There are relatively few studies based on the near-field data following the linear sampling spirit, and we refer to [9] for a near-field reconstruction method by using the Cauchy data and by combining the linear sampling method and the reciprocal gap functional. The integral equation (1.5) is also similar to the one used in the enclosure method originated by Ikehata in [21] and [22]. However, the decaying properties of the integral are directly utilized as an indicator function, and to achieve such properties, more complicated complex geometric optics (CGO) waves must be implemented.

The main contribution in this work is to propose a linear sampling type method based on the near-field measurement data using either the DtN map or the NtD map. In our proposed method, we shall show that both the time-harmonic planar waves and the cylindrical waves can meet the reconstruction purpose. On the other hand, we would like to remark that the current study shall pave the way for implementing more sophisticated waves, e.g. the complex spherical waves in [16] to extract more information about the target obstacles. Finally, we would like to emphasize that the indicator function $g(d)$ in (1.5) exhibits some completely new behaviors than those having been considered in literature on linear sampling methods.

Alternatively, our method could be modified to make use of the NtD map. Actually, for the Helmholtz equation (1.1)–(1.2) confined over $\Omega\backslash\bar{D}$, one imposes the following boundary condition on the exterior boundary

$$\frac{\partial u}{\partial \nu} = g \in H^{-1/2}(\partial\Omega) \quad \text{on} \quad \partial\Omega. \tag{1.6}$$

Again we assume that 0 is not an eigenvalue to the problem (1.1)–(1.3). The NtD map Υ_D is defined by

$$\Upsilon_D(g) = u|_{\partial\Omega}, \tag{1.7}$$

where $u \in H^1(\Omega\backslash\bar{D})$ is the unique solution to (1.1), (1.2) and (1.6). The counterpart to (1.5) is given by

$$\int_{\partial\Omega} (\Upsilon_D - \Upsilon_0) u(x;d) g(d) ds(d) = G_N(x,z), \tag{1.8}$$

where Υ_0 is the NtD map without the inclusion D. The function $G_N(x,z)$ is a Green's function for the Helmholtz equation on Ω with a vanishing Neumann boundary value on $\partial\Omega$.

The rest of the paper is organized as follows. In Section 2, we develop our reconstruction method based on the DtN map. In Section 3, we show how to modify our reconstruction scheme to the case with the NtD map. Section 4 is devoted to the derivation of the explicit forms of Green's functions implemented in our method

when Ω is a disk with radium R. In Section 5, we shall conduct extensive numerical experiments to illustrate the effectiveness of the proposed method. In Section 6, we conclude the work and point out some further directions in the future.

2 Reconstruction by the DtN map

In this section, we develop our reconstruction scheme based on the DtN map using near-field flux measurements. The discussion will be concurrent for both plane waves and cylindrical waves.

The plane wave is of the form

$$w(x,d) = e^{ikx\cdot d} \quad x \in \mathbb{R}^2,$$

where $d \in \mathbb{S}^1$. The corresponding (planar) Herglotz wave function is introduced as

$$(Hg)(x) := w_g(x) = \int_{\mathbb{S}^1} e^{ikx\cdot d} g(d) ds(d) \quad x \in \mathbb{R}^2, \tag{2.1}$$

where $g(d) \in L^2(\mathbb{S}^1)$. We also define

$$U_p := \left\{ w_g(x) \mid w_g(x) = \int_{\mathbb{S}^1} e^{ikx\cdot d} g(d) ds(d),\ g(d) \in L^2(\mathbb{S}^1) \right\}. \tag{2.2}$$

In two dimensions, the cylindrical wave, which has been extensively addressed in [5] and [6], is of the form

$$w(x,d) = J_n(k|x-y|)e^{in\hat{\phi}} \quad x \in \mathbb{R}^2, \tag{2.3}$$

where $J_n(t), t \in \mathbb{R}$ is the n-th order Bessel function, and in polar coordinates, $y = |y|e^{i\phi'} \in \partial\Omega$, $d = y/|y| = e^{i\phi'} \in \mathbb{S}^1$, $x = |x|e^{i\phi} \in \mathbb{R}^2$, $x - y = |x-y|e^{i\hat{\phi}}$.

In the sequel, we simply choose the artificial domain $\Omega = B(0,R)$, namely a central disk of radius R, and focus on the development of the new reconstruction scheme. However, all our subsequent results hold with only slight modifications when Ω is a star-shaped C^2 domain as described in the Introduction. It is worth noting that when n is relatively large, $J_n(k|x-y|)e^{in\hat{\phi}}$ decreases quickly in the vicinity of the fixed source point $y \in \partial\Omega$, and if the obstacle is very small compared with the effective interaction size of the cylindrical wave, the interaction between cylindrical wave and the obstacle will be very weak. Hence, the cases with the orders being $n = 0$, 1, 2, or 3 are of more practical importance, even though our method is irrelevant of these.

Define the Bessel-Herglotz wave function as follows

$$(Bg)(x) := w_g(x) = \int_{\mathbb{S}^1} J_n(k|x-y|)e^{in\hat{\phi}} g(d) ds(d) \quad x \in \mathbb{R}^2, \tag{2.4}$$

where $g(d) \in L^2(\mathbb{S}^1)$. Similar to (2.2), we define

$$U_b := \left\{ w_g(x) \mid w_g(x) = \int_{\mathbb{S}^1} J_n(k|x-y|)e^{in\hat{\phi}} g(d) ds(d),\ g(d) \in L^2(\mathbb{S}^1) \right\}. \tag{2.5}$$

Note that knowing Λ_D is equivalent to knowing the Cauchy data $(u|_{\partial\Omega}, \frac{\partial u}{\partial \nu}|_{\partial\Omega})$. In the following, we shall make use of the linear plane waves $u|_{\partial\Omega} := e^{ikx\cdot d}|_{\partial\Omega}$ as inputs or cylindrical waves $u|_{\partial\Omega} = J_n(k|x-y|)e^{in\hat{\phi}}|_{\partial\Omega}$ as injected boundary sources.

In light of the linear superposition of the Helmholtz system, we establish another pair of solutions to the Helmholtz equation.

Lemma 2.1. *Let $u(x;d) \in H^1(\Omega\backslash\bar{D})$ be the solution to the Helmholtz equation (1.1)–(1.3) associated with the Dirichlet boundary value $f(x,d) = w(x,d)|_{\partial\Omega}$ with $w(x,d) = e^{ikx\cdot d}$ or $w(x,d) = J_n(k|x-y|)e^{in\hat{\phi}}$. Let w_g be a Herglotz wave function (planar or Bessel, resp.). Then the solution to*

$$\begin{cases} (\Delta + k^2)u = 0 \quad in \quad \Omega\backslash\bar{D}, \\ u|_{\partial D} = 0, \quad u|_{\partial\Omega} = w_g|_{\partial\Omega}, \end{cases} \tag{2.6}$$

is given by

$$u_g(x) = \int_{\mathbb{S}^1} u(x;d)g(d)ds(d).$$

The proof of Lemma 2.1 is a direct consequence of the well-posedness and linearity of the involved boundary value problems. We shall also need to consider the following boundary value problem,

$$\begin{cases} (\Delta + k^2)v(x,d) = 0 \quad \text{in} \quad \Omega\backslash\bar{D}, \\ v|_{\partial D} = -f(x,d), \quad v|_{\partial\Omega} = 0. \end{cases} \tag{2.7}$$

It is straightforward to see that $v(x,d) = u(x,d) - w(x,d)$. Similarly to Lemma 2.1, we have

Lemma 2.2. *Let $v(x;d) \in H^1(\Omega\backslash\bar{D})$ be the solution to the Helmholtz equation (2.7) associated with $f(x,d) = e^{ikx\cdot d}$ or $f(x,d) = J_n(k|x-y|)e^{in\hat{\phi}}$. Let w_g be a Herglotz wave function (planar or Bessel, resp.). Then the solution to*

$$\begin{cases} (\Delta + k^2)v = 0 \quad in \quad \Omega\backslash\bar{D}, \\ v|_{\partial D} = -w_g|_{\partial D}, \quad v|_{\partial\Omega} = 0, \end{cases} \tag{2.8}$$

is given by

$$v_g(x) = \int_{\mathbb{S}^1} v(x;d)g(d)ds(d).$$

Since $v(x;d) = u(x;d) - w(x,d)$ in $\Omega\backslash\bar{D}$, we point out the following pivotal relation for our subsequent discussion

$$\left.\frac{\partial v(x;d)}{\partial \nu(x)}\right|_{\partial\Omega} = \Lambda_D(f(x;d)) - \Lambda_0(f(x,d)). \tag{2.9}$$

Next we introduce some function spaces:

$$\begin{aligned} H^1_\Delta(\Omega\backslash\bar{D}) :=& \{\, u \in H^1(\Omega\backslash\bar{D}) \;\mid\; (\Delta + k^2)u = 0 \text{ in } \Omega\backslash\bar{D} \text{ and } u|_{\partial\Omega} = 0 \,\}; \\ H^{-1/2}_\Delta(\partial\Omega) :=& \left\{ \left.\frac{\partial u}{\partial \nu}\right|_{\partial\Omega} \;\mid\; u \in H^1_\Delta(\Omega\backslash\bar{D}) \right\}, \end{aligned}$$

where the boundary values $\frac{\partial u}{\partial \nu}|_{\partial\Omega}$ and $u|_{\partial\Omega}$ are all understood in the sense of traces. Both $H^1_\Delta(\Omega\backslash\bar{D})$ and $H^{-1/2}_\Delta(\partial\Omega)$ are Banach spaces. Then we introduce two operators. We define $S : L^2(\mathbb{S}^1) \to H^1_\Delta(\Omega\backslash\bar{D})$ by

$$Sg(x) := \int_{\mathbb{S}^1} v(x;d)g(d)ds(d) \tag{2.10}$$

and $L : L^2(\mathbb{S}^1) \to H^{-1/2}_\Delta(\partial\Omega)$ by

$$Lg(x) := \int_{\mathbb{S}^1} \frac{\partial v(x;d)}{\partial \nu(x)} g(d)ds(d). \tag{2.11}$$

Noting equation (2.8), we see $Sg(x)|_{\partial D} = -v_g(x)|_{\partial D}$ and $Sg(x)|_{\partial\Omega}$=0. Also by the definitions of S and L we have $\left.\frac{\partial Sg}{\partial \nu}(x)\right|_{\partial\Omega} = Lg(x)$.

The following theorem plays a key role in the mathematical justification of our proposed reconstruction scheme.

Theorem 2.3. *The operator $L : L^2(\mathbb{S}^1) \to H^{-1/2}_\Delta(\partial\Omega)$ is a compact linear operator. If k^2 is not a Dirichlet eigenvalue for $-\Delta$ in $\Omega\backslash\bar{D}$, Ω and D respectively, then L is injective and has a dense range in $H^{-1/2}_\Delta(\partial\Omega)$.*

Before preceding with our proof of Theorem 2.3, we first show the following important result.

Lemma 2.4. *With respect to the $H^{1/2}(\partial D)$-norm, the traces of Herglotz wave functions (or the Bessel Herglotz wave functions) are dense in the space of the traces of the solutions to the Helmholtz equation on ∂D.*

Proof. Consider a solution $u \in H^1(D)$ to the Helmholtz equation $\Delta u + k^2 u = 0$ in D. By Theorem 7.3 in [24], for every $\varepsilon > 0$, there exists a Herglotz wave function w_g such that $\|w_g - u\|_{H^1(D)} \le \varepsilon$, which implies

$$\|w_g - u\|_{H^{1/2}(\partial D)} \le C_1 \|w_g - u\|_{H^1(D)} \le C_1 \varepsilon$$

for some positive constant C_1 by the trace theorem, hence proves the desired density.

For the case with cylindrical waves and the corresponding Bessel-Herglotz wave functions, it suffices for us to show that U_b is dense in $H^1(\Omega)$. Then by the Runge's approximation result (cf. [24, Theorem 7.2]), we can conclude that U_b is dense in $H^1(D)$, and hence by the trace theorem we obtain the desired denseness result for the Bessel-Herglotz wave functions. We shall make use of the additional theorem to prove the denseness of U_b (cf. [8, Appendix D.3]),

$$J_n(k|x-y|)e^{in\hat{\phi}} = \sum_{m=-\infty}^{\infty} J_{m-n}(k|y|)J_m(k|x|)e^{im\phi - i(m-n)\phi'}, \tag{2.12}$$

where $x = |x|e^{i\phi}, y = |y|e^{i\phi'}, x - y = |x-y|e^{i\hat{\phi}}$. Since U_p is dense in $H^1(\Omega)$ (cf. [24]), we only need to prove that U_b is dense in U_p with respect to the $H^1(\Omega)$-norm.

To that end, we first note that $v(x) \in U_p$ iff $v(x) = \sum_{n=-\infty}^{\infty} a_n J_n(k|x|)e^{in\phi}$ with $\{a_n, n \in \mathbb{Z}\} \in l^2$ (cf. [4] and [12]). For arbitrary fixed $\varepsilon > 0$, let N be a sufficiently large integer such that

$$\|v(x) - \sum_{n=-N}^{N} a_n J_n(k|x|)e^{in\phi}\|_{H^1(\Omega)} \leq \varepsilon. \tag{2.13}$$

Next, set

$$g(d) = \sum_{l=-N}^{N} \frac{a_l e^{i(l-n)\phi'}}{2\pi J_{l-n}(kR)}.$$

It is straightforward to calculate that

$$\|g(d)\|^2_{L^2(\mathbb{S}^1)} = \sum_{l=-N}^{N} \frac{a_l^2}{J_{l-n}(kR)^2}$$

and hence $g(d) \in L^2(\mathbb{S}^1)$. Furthermore, by using (2.12), together with direct calculations, one can show

$$u(x) := \int_{\mathbb{S}^1} J_n(k|x-y|)e^{in\hat{\phi}}g(d)ds(d) = \sum_{n=-N}^{N} a_n J_n(k|x|)e^{in\phi}, \tag{2.14}$$

which by (2.13) gives

$$\|u - v\|_{H^1(\Omega)} < \varepsilon. \tag{2.15}$$

Clearly, $u \in U_b$ and hence (2.15) indicates that U_b is dense in U_p with respect to the $H^1(\Omega)$-norm. This completes the proof of Lemma 2.4. □

Proof of Theorem 2.3. We first prove the compactness of operator L. Consider a function $g \in L^2(\mathbb{S}^1)$ and set $h = Lg$. Noting that D and Ω are respectively of C^2 and C^∞ class, and $-w_g$ is infinitely differentiable on ∂D, we know $Sg \in H^2(\Omega\backslash\bar{D})$ and $h \in H^{1/2}(\partial\Omega)$ by the well-posedness of system (2.8). Then we need only to prove the existence of a constant $\hat{C}$ such that $\|Lg\|_{H^{1/2}(\partial\Omega)} \leq \hat{C}\|g\|_{L^2(\mathbb{S}^1)}$, since the natural injection from $H^{1/2}(\partial\Omega)$ to $H^{-1/2}(\partial\Omega)$ is compact. By the trace theorem we have $\|h\|_{H^{1/2}(\partial\Omega)} < C_2\|Sg\|_{H^2(\Omega\backslash\bar{D})}$ for some constant C_2. Then by the a priori estimate of the solution to (2.8) there exists a positive constant C_1 such that $\|Sg\|_{H^2(\Omega\backslash\bar{D})} \leq C_1\|w_g\|_{H^{3/2}(\partial D)}$. Noting that w_g is also a solution of the Helmhlotz equation in $H^2(D)$, and hence by the trace theorem, there exists a constant C_3, such that $\|w_g\|_{H^{3/2}(\partial D)} \leq C_3\|w_g\|_{H^2(D)}$. Noting that both $e^{ikx\cdot d}$ and $J_n(k|x-y|)e^{in\hat{\phi}}$ are analytic, it is straightforward to see the boundedness of the mapping $g \mapsto w_g$ from $L^2(\mathbb{S}^1)$ into $H^2(D)$, that is, there exists a constant C_4, such that $\|w_g\|_{H^2(D)} \leq C_4\|g\|_{L^2(\mathbb{S}^1)}$. This proves the boundedness of L by the constant $\hat{C} = C_2C_1C_3C_4$.

Next we show the injectivity of L. Suppose $g \in L^2(\mathbb{S}^1)$ and $Lg = 0$. Clearly, $Sg|_{\partial\Omega} = 0$ and $\frac{\partial Sg}{\partial\nu}|_{\partial\Omega} = Lg = 0$. Hence, by the unique continuation, we know $Sg = 0$

in $\Omega\backslash\bar{D}$. Therefore, $w_g|_{\partial D} = -Sg|_{\partial D} = 0$. Then, noting w_g is a solution for the Helmholtz equation in $H^1(D)$ and k^2 is not a Dirichlet eigenvalue, we see $w_g = 0$ in D. By unique continuation again, we see $w_g = 0$ in $\mathbb{R}^2$. If $w_g \in U_p$, then by Theorem 3.15 in [12], $g(d) = 0$. If $w_g \in U_b$, we can write $g(d) = \sum_{l=-\infty}^{\infty} a_l e^{il\phi'}$ with $\{a_l\}_{l\in\mathbb{Z}} \in l^2$ by Fourier expansion, then it follows from direct calculations that

$$w_g(x) = \sum_{l=-\infty}^{\infty} 2\pi a_{l-n} J_{l-n}(kR) J_l(k|x|) e^{il\phi}. \tag{2.16}$$

It is straightforward to verify by using the asymptotic properties of Bessel functions that $\sum_{l=-N}^{N} 2\pi a_{l-n} J_{l-n}(kR) J_l(k|x|) e^{il\phi}$ is absolutely convergent in $H^1(\Omega)$ as $N \to \infty$. Then by (2.16) and $w_g|_{\partial\Omega} = 0$, we see $a_{l-n} J_{l-n}(kR) J_l(kR) = 0$. By further noting k^2 is not an Dirichlet eigenvalue for Ω, which implies $J_n(kR) \neq 0$ for arbitrary n, we have $a_l = 0$ for all $l \in \mathbb{Z}$. That is, $g = 0$.

Finally, we show that L has a dense range in $H_\Delta^{-1/2}(\partial\Omega)$. For every $\phi \in H_\Delta^{-1/2}(\partial\Omega)$, let $u \in H_\Delta^1(\Omega\backslash\bar{D})$ be such that $\frac{\partial u}{\partial \nu}|_{\partial\Omega} = \phi|_{\partial\Omega}$. Then by Lemma 2.4, there exists a (planar or Bessel, resp.) Herglotz wave function w_g such that for arbitrary small $\varepsilon > 0$, $\|w_g - u\|_{H^{1/2}(\partial D)} \leq \varepsilon$. By the well-posedness of the boundary value problem (2.8), we see $\|Sg - u\|_{H^1(\Omega\backslash\bar{D})} \leq C_1\varepsilon$. By the trace theorem, we further have a constant $C_2 > 0$ such that $\|Lg - \phi\|_{H^{-1/2}(\partial\Omega)} < C_2\|Sg - u\|_{H^1(\Omega\backslash\bar{D})} \leq C_2C_1\varepsilon$. This proves Theorem 2.3. □

For any $x \in \bar{\Omega}$ and $z \in \Omega$, let $G(x, z)$ be a Green's function associated with the Helmholtz equation with a vanishing Dirichlet value on $\partial\Omega$. For our reconstruction algorithm developed in the sequel, we take $G(x, z) = \Phi(x, z) - u(x, z)$, where $\Phi(x, z) = \frac{i}{4}H_0^{(1)}(k|x-z|)$ is the fundamental solution to the operator $-\Delta - k^2$ and $u(x, z)$ satisfies

$$(\Delta + k^2)u(x, z) = 0 \quad \text{in } \Omega, \quad u(x, z)|_{\partial\Omega} = \Phi(x, z)|_{\partial\Omega}, \tag{2.17}$$

for any fixed $z \in \Omega$. For the case with Ω being a central disk, an explicit form of $G(x, z)$ can be derived in the way demonstrated in Section 4. It is clear to see that $G(x, z) \in H_\Delta^1(\Omega\backslash\bar{D})$ if $z \in D$, which further implies $\frac{\partial G(x,z)}{\partial \nu(x)}|_{\partial\Omega} \in H_\Delta^{-1/2}(\partial\Omega)$ if $z \in D$.

Now we are ready to present the first main theorem and establish the reconstruction algorithm. To that end, we introduce the following crucial first kind integral equation for $g_z \in L^2(\mathbb{S}^1)$:

$$(Lg_z)(x) = \frac{\partial G(x, z)}{\partial \nu(x)}, \quad x \in \partial\Omega, \ z \in \Omega, \tag{2.18}$$

which by (2.9) is equivalent to

$$\int_{\partial\Omega} (\Lambda_D - \Lambda_0)(f(x; d)) g_z(d) ds(d) = \frac{\partial G(x, z)}{\partial \nu(x)}, \quad x \in \partial\Omega, \ z \in \Omega\,. \tag{2.19}$$

Theorem 2.5. *For g^z in (2.18) or (2.19), we have*

(i) If $z \in D$, then for every $\varepsilon > 0$, there exists $g_{z,\varepsilon} \in L^2(\mathbb{S}^1)$ such that

$$\|Lg_{z,\varepsilon}(x) - \frac{\partial G(x,z)}{\partial \nu(x)}\|_{H^{-1/2}(\partial\Omega)} \leq \varepsilon. \tag{2.20}$$

Moreover, for every $z^* \in \partial D$ and every choice of $g_{z,\varepsilon} \in L^2(\mathbb{S}^1)$ in (2.20),

$$\lim_{z\to z^*} \|g_{z,\varepsilon}\|_{L^2(\mathbb{S}^1)} = \infty \quad \text{and} \quad \lim_{z\to z^*} \|v_{g_{z,\varepsilon}}\|_{H^1(D)} = \infty. \tag{2.21}$$

(ii) If $z \in \Omega\backslash\bar{D}$, we can solve (2.18) by the Tiknonov regularization to have a regularized solution $g_{z,\varepsilon}$ in $L^2(\mathbb{S}^1)$, depending on a regularizer $\varepsilon > 0$. That is, $g_{z,\varepsilon}$ is the unique solution to the regularized system

$$(\varepsilon I + L^*L)\, g = L^* \frac{\partial G(\cdot, z)}{\partial \nu}\,. \tag{2.22}$$

Moreover, only one of the following two possibilities occurs to the sequence $\{g_{z,\varepsilon}\}$: either there exists a sequence $\varepsilon_n \to 0^+$ such that

$$\lim_{\varepsilon_n\to 0^+} \|Lg_{z,\varepsilon_n}(x) - \frac{\partial G(x,z)}{\partial \nu(x)}\|_{H^{-1/2}(\partial\Omega)} = 0, \tag{2.23}$$

and

$$\lim_{\varepsilon_n\to 0^+} \|g_{z,\varepsilon_n}\|_{L^2(\mathbb{S}^1)} = \infty; \tag{2.24}$$

or, there exists a constant $C > 0$ such that for all $\varepsilon > 0$,

$$\|Lg_{z,\varepsilon}(x) - \frac{\partial G(x,z)}{\partial \nu(x)}\|_{H^{-1/2}(\partial\Omega)} \geq C. \tag{2.25}$$

Remark 2.6. *Part (ii) of Theorem 2.5 tells that the following situation would not happen: there exists a sequence $\varepsilon_n \to 0^+$ such that*

$$\lim_{\varepsilon_n\to 0^+} \|Lg_{z,\varepsilon_n}(x) - \frac{\partial G(x,z)}{\partial \nu(x)}\|_{H^{-1/2}(\partial\Omega)} = 0, \tag{2.26}$$

and

$$\liminf_{\varepsilon_n\to 0^+} \|g_{z,\varepsilon_n}\|_{L^2(\mathbb{S}^1)} < \infty. \tag{2.27}$$

More precisely, we may interpret it as follows: for any point z lying outside the obstacle, either the magnitude of its indicator function g_{z,ε_n} blows up, or the magnitude of the residual $Lg_{z,\varepsilon_n} - \frac{\partial G(\cdot,z)}{\partial \nu(x)}$ is bounded from below by a positive constant.

Proof of Theorem 2.5. We first verify (i). For $z \in D$, we obviously have $G(\cdot, z)|_{\partial D} \in H^{1/2}(\partial D)$. Hence by Lemma 2.4, for any $\varepsilon > 0$ there exists $g_{z,\varepsilon} \in L^2(\mathbb{S}^1)$ such that

$$\|v_{g_{z,\varepsilon}} - G(\cdot, z)\|_{H^{1/2}(\partial D)} \leq \varepsilon\,. \tag{2.28}$$

In the rest of the proof, we let C denote a generic positive constant, which may differ at different estimates but is fixed and finite in a single relation. Since $v_{g_{z,\varepsilon}} = Sg_{z,\varepsilon}$ on ∂D and $G(\cdot, z) \in H^1_\Delta(\Omega\backslash\bar{D})$, by the well-posedness of problem (2.8) we have $\|Sg_{z,\varepsilon} - G(\cdot, z)\|_{H^1(\Omega\backslash\bar{D})} \leq C\varepsilon$. This, along with the trace theorem and the fact that $\partial Sg/\partial\nu = Lg$ on $\partial\Omega$, leads to the desired estimate (2.20).

We next show (2.21). By the trace theorem again,

$$\|Sg_{z,\varepsilon} - G(\cdot, z)\|_{H^{1/2}(\partial D)} \leq C\|Sg_{z,\varepsilon} - G(\cdot, z)\|_{H^1(\Omega\backslash\bar{D})}. \tag{2.29}$$

Assume contrarily that there exists $z^* \in \partial D$, $0 < M < \infty$ and a sequence $z_n \to z^*$ such that $\|v_n\|_{H^1(D)} \leq M$, where we write $v_n := v_{g_{z_n,\varepsilon}}$. Then by (2.28) we have

$$\|G(\cdot, z_n)\|_{H^{1/2}(\partial D)} \leq \|G(\cdot, z_n) - v_n\|_{H^{1/2}(\partial D)} + \|v_n\|_{H^{1/2}(\partial D)} \leq C(\varepsilon + M) \tag{2.30}$$

for all $n > 0$. However, noting that $G(\cdot, z)$ has the same singularity as the fundamental solution $\Phi(\cdot, z)$, we have $\|G(\cdot, z_n)\|_{H^1(U\backslash\bar{D})} \to \infty$ as $n \to \infty$ for any bounded region U containing D. This contradicts to (2.30), thus proves the second statement in (2.21). The first statement follows directly from the boundedness of the mapping $g \mapsto v_g|_D$ from $L^2(\mathbb{S}^1)$ into $H^1(D)$.

Next, we demonstrate (ii). For a point $z \in \Omega \setminus D$ and small $\varepsilon > 0$, we introduce the Tiknonov functional $J_{z,\varepsilon} : L^2(\mathbb{S}^1) \to \mathbb{R}$ by

$$J_{z,\varepsilon}(g) = \|Lg - \frac{\partial G(\cdot, z)}{\partial\nu}\|^2_{H^{-1/2}(\partial\Omega)} + \varepsilon\|g\|^2_{L^2(\mathbb{S}^1)}$$

for $g \in L^2(\mathbb{S}^1)$. By the classical result on the regularities of solutions to (2.7) (cf. [18]), we know the operator L has a continuous kernel and hence L^*L is compact from $L^2(\mathbb{S}^1)$ to $L^2(\mathbb{S}^1)$. Moreover, $L^*L + \varepsilon I$ is positive since L is injective by Theorem 2.3. Therefore for any $\varepsilon > 0$, there exists a unique minimizer $g_{z,\varepsilon} \in L^2(\mathbb{S}^1)$ to functional $J_{z,\varepsilon}$, which is given by (2.22). Now it suffices for us to show that (2.26) and (2.27) can not hold simultaneously. Assume contrarily that both (2.26) and (2.27) are true, then we have a sequence $\{g_{z,\varepsilon_n}\}$ such that $\varepsilon_n \to 0^+$ as $n \to \infty$, and $\|g_{z,\varepsilon_n}\|_{L^2(\mathbb{S}^1)} \leq C$ for all n and (2.26) also holds. Then there exists a subsequence $g_{z,\varepsilon_{n'}}$ which converges weekly to some $g \in L^2(\mathbb{S}^1)$. By the compactness of L, we have $Lg_{z,\varepsilon_{n'}} \to Lg$ in $H^{-1/2}_\Delta(\partial\Omega)$, which implies $Lg(x) = \frac{\partial G(x,z)}{\partial\nu(x)}|_{\partial\Omega}$ by means of (2.26). Therefore we obtain $\frac{\partial Sg}{\partial\nu} = Lg$ and $Sg(x) = G(x, y)$ on $\partial\Omega$. Using Holmgren's uniqueness theorem, we see $Sg(x) = G(x, z)$ in a neighborhood of $\partial\Omega$. By the unique continuation principle, we further have $Sg(x) = G(x, z)$ in $\Omega\backslash(\bar{D}\bigcup\{z\})$. However this is impossible, since $Sg(x) \in H^1(\Omega\backslash\bar{D}) \cup H^1(\Omega\backslash(\bar{D}\bigcup\{z\})$, but $G(x, z)$ does not belong to $H^1(\Omega\backslash(\bar{D}\bigcup\{z\})$ for $z \in \Omega\backslash D$. This proves (ii), hence completes the proof of Theorem 2.5. □

Theorem 2.5 suggests a possible procedure to determine if a point $z \in \Omega$ lies in D or not. To do so, we may choose two cut-off values $c_1, c_2 > 0$. Then one can first find a Tikhonov regularized solution $g_{z,\varepsilon}$ to (2.18). If $\|g_{z,\varepsilon}\|_{L^2(\mathbb{S}^1)} > c_1$, we count $z \notin D$; Otherwise we further compute the residual $Lg_{z,\varepsilon} - \partial G(\cdot, z)/\partial\nu$. If the norm of this residual is less than c_2, we count $z \in D$, or $z \notin D$ otherwise.

The above discussion leads us to the following numerical reconstruction scheme.

Numerical Reconstruction Scheme (DtN)
Select two cut-off values $c_1, c_2 > 0$.

Step 1. Collect the measurement data $\frac{\partial u(x;d)}{\partial \nu}$ on $\partial\Omega$ corresponding to the excitation $f(x,d)$ on $\partial\Omega$ for different d's .

Step 2. Select a sampling mesh $\mathcal{T}_h$ over the domain Ω.

Step 3. For each sampling mesh point $z \in \mathcal{T}_h$, compute a Tikhonov regularized solution $g_{z,\varepsilon}$ to (2.18).

Step 4. If $\|g_{z,\varepsilon}\|_{L^2(\mathbb{S}^1)} > c_1$, we count $z \notin D$; otherwise we compute the residual $Lg_{z,\varepsilon} - \partial G(\cdot, z)/\partial\nu$. If the norm of this residual is less than c_2, we count $z \in D$; otherwise we count $z \notin D$.

3 Reconstruction by the NtD map

We proposed a reconstruction scheme of a unknown obstacle in the previous section by the DtN map. Similar ideas work as well for the NtD map. In this section we present some necessary modifications for the case with the NtD map. Let $u(x,d) \in H^1(\Omega\backslash\bar{D})$ be the unique solution to the system

$$\begin{cases} (\Delta + k^2)u(x,d) = 0 \ \text{ in } \Omega\backslash\bar{D}, \\ u = 0 \text{ on } \partial D; \quad \partial u/\partial\nu = \partial w(\cdot,d)/\partial\nu \text{ on } \partial\Omega, \end{cases} \tag{3.1}$$

where $w(x,d)$ is the (planar or cylindrical) incident wave as introduced in Section 2. Here it is assumed that k^2 is not a Neumann eigenvalue to $-\Delta$ in Ω and 0 is not an eigenvalue to the problem (3.1). We also set $v(x,d) = u(x,d) - w(x,d)$, then $v(x,d)$ satisfies

$$\begin{cases} (\Delta + k^2)v(x,d) = 0 \ \text{ in } \Omega\backslash\bar{D}, \\ v = -w(x,d) \text{ on } \partial D; \quad \partial v/\partial\nu = 0 \text{ on } \partial\Omega. \end{cases} \tag{3.2}$$

The NtD map associated with (3.1) is given by

$$\Upsilon_D \left(\frac{\partial w(x,d)}{\partial \nu}\bigg|_{\partial\Omega} \right) = u(x,d)|_{\partial\Omega}.$$

When the inclusion D is empty, we shall write Υ_D as Υ_0.

Similarly to Lemmata 2.1 and 2.2, we have the following result by linear superposition.

Proposition 3.1. *Let $u(x,d)$ and $v(x,d) \in H^1(\Omega\backslash\bar{D})$ be the solution to (3.1) and (3.2) respectively associated with $w(x,d)$, and w_g be a Herglotz wave function (planar and Bessel resp.). Then the solutions to the system*

$$\begin{cases} (\Delta + k^2)u(x,d) = 0 \quad in \quad \Omega\backslash\bar{D}, \\ u|_{\partial D} = 0, \quad \frac{\partial u}{\partial\nu}|_{\partial\Omega} = \frac{\partial w_g}{\partial\nu}|_{\partial\Omega} \end{cases} \tag{3.3}$$

and

$$\begin{cases} (\Delta + k^2)v(x,d) = 0 \quad in\ \Omega\backslash\bar{D}, \\ v|_{\partial D} = -w_g|_{\partial D}, \quad \frac{\partial v}{\partial \nu}|_{\partial\Omega} = 0 \end{cases} \tag{3.4}$$

are respectively given by

$$u_g(x) = \int_{\mathbb{S}^1} u(x;d)g(d)ds(d) \quad and \quad v_g(x) = \int_{\mathbb{S}^1} v(x;d)g(d)ds(d)\,.$$

For the subsequent analysis, we introduce the following function spaces

$$\hat{H}^1_\Delta(\Omega\backslash\bar{D}) := \{\, u \in H^1(\Omega\backslash\bar{D});\ (\Delta + k^2)u = 0 \text{ in } \Omega\backslash\bar{D} \text{ and } \frac{\partial u}{\partial \nu}|_{\partial\Omega} = 0\,\},$$
$$\hat{H}^{1/2}_\Delta(\partial\Omega) := \{\, u|_{\partial\Omega};\ u \in \hat{H}^1_\Delta(\Omega\backslash\bar{D})\,\}$$

and the operator $\hat{S} : L^2(\mathbb{S}^1) \to \hat{H}^{1/2}_\Delta(\partial\Omega)$ defined by

$$\hat{S}g(x) := v_g(x)|_{\partial\Omega} = \int_{\mathbb{S}^1} v(x;d)g(d)ds(d)|_{\partial\Omega}, \tag{3.5}$$

where $v_g(x)$ is the solution to (3.4). Similarly to Theorem 2.3, we have

Theorem 3.2. *The operator $\hat{S} : L^2(\mathbb{S}^1) \to \hat{H}^{1/2}_\Delta(\partial\Omega)$ is compact and has a dense range. Furthermore, $\hat{S}$ is injective provided that k^2 is not a Dirichlet eigenvalue to $-\Delta$ in both D and Ω.*

Let $G_N(x,z)$, $x \in \bar{\Omega}, z \in \Omega$, be a Green's function for the Helmholtz equation with a homogeneous Neumann condition on $\partial\Omega$. For the convenience, we will take $G_N(x,z) = \Phi(x,z) - u(x,z)$, where $\Phi(x,z)$ is the fundamental solution to $-\Delta - k^2$ for any fixed z, and $u(x,z)$ satisfies

$$(\Delta + k^2)u(x,z) = 0 \quad \text{in } \Omega; \quad \frac{u(x,z)}{\partial\nu} = \frac{\partial\Phi(x,z)}{\partial\nu} \quad \text{on } \partial\Omega \tag{3.6}$$

for any fixed $z \in \Omega$. When Ω is a simple disk, we will derive the explicit expression of $G_N(x,z)$ in Section 4.

Now we are ready to present a major theorem of this section, a counterpart to Theorem 2.5 based on the NtD map; and its proof follows the one of Theorem 2.5, with slight modifications. The governing equation involved in the theorem is now given by

$$\hat{S}g_z(x) = G_N(x,z), \quad x \in \partial\Omega,\ z \in \Omega, \tag{3.7}$$

or equivalently,

$$\int_{\partial\Omega} (\Upsilon_D - \Upsilon_0)(\frac{\partial w(x;d)}{\partial\nu}\Big|_{\partial\Omega})g_z(d)ds(d) = G_N(x,z), \quad x \in \partial\Omega,\ z \in \Omega.$$

Theorem 3.3. *For g^z in (3.7), we have*

(i) If $z \in D$, then for every $\varepsilon > 0$ there exists $g_{z,\varepsilon}$ to (3.7) such that

$$\|\hat{S} g_{z,\varepsilon}(x) - G_N(x,z)\|_{H^{1/2}(\partial\Omega)} \leq \varepsilon. \tag{3.8}$$

Moreover, for every $z^* \in \partial D$ and every choice of $g_{z,\varepsilon} \in L^2(\mathbb{S}^1)$ in (3.8),

$$\lim_{z \to z^*} \|g_{z,\varepsilon}\|_{L^2(\mathbb{S}^1)} = \infty \quad \textit{and} \quad \lim_{z \to z^*} \|v_{g_{z,\varepsilon}}\|_{H^1(D)} = \infty. \tag{3.9}$$

(ii) If $z \in \Omega \backslash \bar{D}$, we can solve(3.7) by the Tiknonov regularization to have a regularized solution $g_{z,\varepsilon}$ in $L^2(\mathbb{S}^1)$, depending on a regularizer ε. That is, $g_{z,\varepsilon}$ is the unique solution to the system

$$(\varepsilon I + \hat{S}^* \hat{S}) g = \hat{S}^* G_N(\cdot, z). \tag{3.10}$$

Moreover, only one of the following two possibilities occurs to the sequence $\{g_{z,\varepsilon}\}$: either there exists a sequence $\varepsilon_n \to 0^+$ such that

$$\lim_{\varepsilon_n \to 0^+} \|\hat{S} g_{z,\varepsilon_n}(x) - G_N(x,z)\|_{H^{1/2}(\partial\Omega)} = 0 \tag{3.11}$$

and

$$\lim_{\varepsilon_n \to 0^+} \|g_{z,\varepsilon_n}\|_{L^2(\mathbb{S}^1)} = \infty\,; \tag{3.12}$$

or, there exists a positive constant C such that for all $\varepsilon > 0$,

$$\|\hat{S} g_{z,\varepsilon}(x) - G_N(x,z)\|_{H^{1/2}(\partial\Omega)} \geq C. \tag{3.13}$$

Similarly to our discussion in Section 2 for the motivation of the Numerical Reconstruction Scheme (DtN) by Theorem 2.5, Theorem 3.3 above suggests us the following reconstruction scheme by using the NtD map.

Numerical Reconstruction Scheme (NtD)
Select two cut-off values $c_1, c_2 > 0$.

Step 1. Collect the measurement data $u(x;d)$ on $\partial\Omega$ corresponding to $\partial w(x,d)/\partial\nu$ on $\partial\Omega$ for different d's.

Step 2. Select a sampling mesh $\mathcal{T}_h$ over the domain Ω.

Step 3. For each sampling point $z \in \mathcal{T}_h$, compute a Tikohnov regularized solution $g_{z,\varepsilon}$ to the equation (3.7).

Step 4. If $\|g_{z,\varepsilon}\|_{L^2(\mathbb{S}^1)} > c_1$, we count $z \notin D$; otherwise we compute the residual $\hat{S} g_{z,\varepsilon_n}(x) - G_N(x,z)$. If the norm of this residual is less than c_2, we count $z \in D$; otherwise we count $z \notin D$.

Remark 3.4. *If the boundary condition of the obstacle is of general type (1.2), all the results we have obtained in Sections 2 and sec:NtD still hold. In particular, we can show similar density for the Herglotz wave functions (U_p or U_b) in $H^1(\Omega)$ and similar results to Theorem 2.5 and 3.3.*

4 Green's functions

We recall that the Green's functions $G(x,z)$ and $G_N(x,z)$ are involved in our reconstruction schemes developed in the previous sections. In this section we demonstrate that one may find their explicit forms for some domains of special geometry. We shall restrict our discussion on the case that Ω is a disk of radius R centered at the origin. We first recall the fundamental solution $\Phi(x,z) = \frac{i}{4}H_0^{(1)}(k|x-z|)$ associated with the Helmholtz operator $-\Delta - k^2$ and its special representation (cf. [8]):

$$\Phi(x,z) = \frac{i}{4}\sum_{n=-\infty}^{\infty} J_n(k|z|)H_n^{(1)}(k|x|)e^{in(\phi-\phi')}, \tag{4.1}$$

where $|x| > |z|$ and $x = |x|e^{i\phi}$, $z = |z|e^{i\phi'}$ in polar coordinates. Here $H_n^{(1)}(t)$ is the first Hankel function of order n. Noting that $G(x,z) = \Phi(x,z) - u(x,z)$, where $u(x,z)$ solves (2.17). Now we write $u(x,z)$ as

$$u(x,z) = \sum_{n=-\infty}^{\infty} a_n J_n(k|x|)e^{in\phi}. \tag{4.2}$$

By direct computings using the boundary condition in (2.17) and the representation (4.1) we obtain

$$a_n = \frac{iH_n^{(1)}(kR)J_n(k|z|)e^{-in\phi'}}{4J_n(kR)}\,. \tag{4.3}$$

Next, we show that $u(x,z)$ in (4.2) with the corresponding coefficients given by (4.3) is well-defined in $H^1(\Omega)$. Using the following asymptotic behaviors of $J_n(t)$ and $H_n(t)$ for fixed t and sufficiently large n (cf. [1]),

$$J_n(t) \sim \frac{1}{\sqrt{2\pi n}}\cdot(\frac{et}{2n})^n, \quad H_n^{(1)}(t) \sim -i\frac{\sqrt{2}}{\sqrt{\pi n}}\cdot(\frac{2n}{et})^n, \tag{4.4}$$

one can verify that $|a_nJ_n(k|x|)| \sim \frac{1}{4\pi n}\cdot(\frac{|z|}{R})^n\cdot(\frac{|x|}{R})^n$. Using the relation $J_n{}'(t) = \frac{1}{2}(J_{n-1}(t) - J_{n+1}(t))$, one sees that $a_nJ_n{}'(k|x|)$ has a similar asymptotic behavior. Finally, by using these asymptotic results it is straightforward to show that $\sum_{n=-N}^{N} a_nJ_n(k|x|)e^{in\phi}$ converges to $u(x,z)$ in $H^1(\Omega)$ as $N\to\infty$. Hence, the Green's function $G(x,y)$ is given by

$$G(x,z) = \Phi(x,y) - \sum_{n=-\infty}^{\infty}\frac{iH_n^{(1)}(kR)J_n(k|z|)e^{-in\phi'}}{4J_n(kR)}J_n(k|x|)e^{in\phi} \tag{4.5}$$

for $|x| > |z|$ and $x = |x|e^{i\phi}$, $z = |z|e^{i\phi'}$.

In a similar manner, one can find $G_N(x,z)$ by solving (3.6) that

$$G_N(x,z) = \Phi(x,z) - \sum_{n=-\infty}^{\infty}\frac{iH_n^{(1)}{}'(kR)J_n(k|z|)e^{-in\phi'}}{4J_n{}'(kR)}J_n(k|x|)e^{in\phi}, \tag{4.6}$$

for $|x| > |z|$ and $x = |x|e^{i\phi}$, $z = |z|e^{i\phi'}$.

5 Numerical experiments and discussions

In this section, we present some numerical experiments to illustrate the new sampling approach developed in the previous sections to the near-field inverse obstacle scattering problem with some examples. Here are some parameters to be used in this section: R for the radius of the surrounding medium, k for the wave number, δ for the noise level, $d = (d_x, d_y)^T$ for unitary incident direction and $c = (c_x, c_y)^T$ for the object shifting with displacements c_x and c_y.

We shall test three different scatterers for system (1.1)-(1.2): a unit disk of radius 1, a kite-shaped object, which are denoted by **B** and **K**, respectively, and a combination of **B** and **K** (possibly at different locations). The specification of these scatterers can be parameterized as follows:

$$\texttt{Ball:} \qquad x(t) = (\cos t, \sin t), \quad 0 \le t \le 2\pi, \tag{5.1}$$

$$\texttt{Kite:} \qquad x(t) = (\cos t + 0.65\cos 2t - 0.65, 1.5\sin t), \quad 0 \le t \le 2\pi. \tag{5.2}$$

The surrounding medium Ω is always chosen to be a disk with radius $R = 5.5$ centered at the origin. Other shapes of surrounding media are also possible provided the analytical forms of the corresponding Green functions of Dirichlet or Neumann type are available.

We will carry out three groups of numerical tests. The synthetic near-field data of the direct problems are generated by solving the variational equation corresponding to the system (1.1)-(1.2) with isoparametric quadratic finite elements. We solve the discrete system over a family of increasingly finer meshes over the computational domain $\Omega \setminus D$ until the relative error is small, e.g., less than 10^{-3}, which, compared with the noise level we added, is negligible and viewed as noise-free data. Note that the synthetic data from the NtD map are much more accurate than those from the DtN map since the flux data $\frac{\partial u}{\partial \nu}$ converge one order slower in terms of the meshsize than the potential u using the finite element solver in our numerical test. So the NtD mapping should be more reliable and stable by our experience. Thus we will mainly focus on the NtD map afterward.

The near-field measurement data generated along the medium boundary Γ are then subjected pointwise to certain uniform random noise. The uniform random noise in magnitude as well as in direction is added according to the following formula,

$$U = U + \delta r_1 |U| \exp(i\pi r_2)\,, \tag{5.3}$$

where U may denote either kind of measurement data, u or $\frac{\partial u}{\partial \nu}$, r_1 and r_2 are two uniform random numbers, both ranging from -1 to 1, and δ represents the noise level. For each mesh point z, the corresponding integral operator equation is discretized through the mid-point quadrature method at the equidistantly distributed collocation points along the medium boundary Γ. It is worth pointing out that the integral kernel is quite smooth and thus the resulting matrix after discretization is highly ill-posed with condition number ranging from $10^{16} - 10^{18}$. Hence certain regularization is definitely

necessary. Here the linear system is solved by using the Tikhonov regularization technique, with the corresponding regularization parameters determined by the Morozov discrepancy principle.

The measurement data depend on two variables: the observation location $x = (R\cos(\phi),\, R\sin(\phi))$ on the medium boundary Γ with $\phi \in [-\pi, \pi]$, and incident direction $d = (\cos(\theta),\, \sin(\theta))$ from the unit circle in $\mathbb{R}^2$ with $\theta \in [-\pi, \pi]$. We compute the near-field measurement data at 100 equidistantly distributed observation points $x_j = (R\cos\phi_j,\, R\sin\phi_j)$, $\phi_j = 2j\pi/100 - \pi$, $j = 1, 2, \ldots, 100$, corresponding to 100 equidistantly distributed incident directions $d_j = (\cos\theta_j,\, \sin\theta_j)$, $\theta_j = 2j\pi/100 - \pi$, $j = 1, 2, \ldots, 100$, around the surrounding medium circle. We may identify the observation points and incident directions with the index sequence $\{1, 2, \ldots, 100\}$ and illustrate the measurement data by the contour plots of the corresponding 100×100 matrices as shown in the following examples.

Hereafter, the norms of the indicator function g_z and the residual of the integral equation $G_N(x, z) - Sg_z$ in the DtN case (or $\frac{\partial G(x,z)}{\partial \nu(x)} - Lg_z$ in the NtD case) are denoted by *g-norm* and *res-norm*, respectively. Note that theoretically the residuals are defined in $H^{-1/2}$-norm or $H^{1/2}$-norm, which are very difficult to compute at the discrete level. Therefore for the approximation of $H^{1/2}$- and $H^{-1/2}$-norms, one can use the discrete approximation by multiplying a factor $h_F^{-1/2}$ and $h_F^{1/2}$ (frequently used in the discontinuous Galerkin finite element analysis), respectively, as follows:

$$\|w\|^2_{\pm 1/2,h,\Gamma_h} = \sum_{F\in\Gamma_h} h_F^{\mp 1}\|w\|^2_{L^2(F)},$$

where Γ_h is the piecewise approximation to the artificial boundary Γ on the finite element triangulation, F is any line segment on Γ_h with element size h_F. Since we use equi-distant points along the boundary Γ, which implies all h_F in line segments $F \in \Gamma_h$ are the same. Therefore there is a fixed scaling factor involving some fixed meshsize h_F between the fractional $H^{1/2}$-norm (or $H^{-1/2}$-norm) and L^2-norm of the residual, which guarantees that the blowup pattern of those pairs of norms are actually the same. Consequently, we can replace the complicated $H^{1/2}$-norm (or $H^{-1/2}$-norm) by simple discrete L^2-norm, which is simple to calculate and makes the two indicators measured in the uniform L^2 sense. Furthermore, these indicator norms are plotted by transformation via 10-based logarithm for better visualization. It is worth noting that the sampling grid is chosen to be a bit smaller than the surrounding medium disk since the series of $G_N(x, z)$ or $\frac{\partial G(x,z)}{\partial \nu(x)}$ converges very slow as n increases from 0 to $\pm\infty$ when the interior point z approaches some boundary point x by our numerical experience. In practice, one can always choose a slightly larger surrounding medium than necessary to ensure the convergence. In our tests, the fictitious Cartesian grid is chosen to be 101-by-101 uniform grid covering the rectangular region $[-R, R] \times [-R, R]$, while only points within the disk with radius $\frac{4}{5}R$ and centered at the origin are sampled for computation, and the other points are specified by a constant value much larger than the cut-off value.

Example 1. Unit disk obstacle with $c = (-1.5, -1.5)^T$.

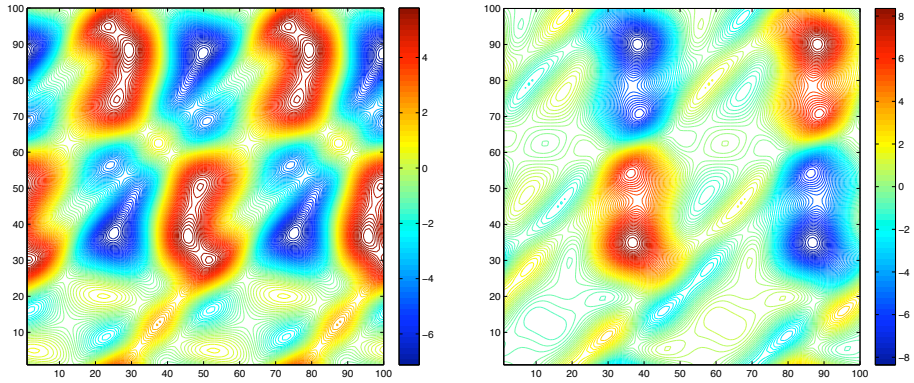

(a) (b)

Figure 1: Contour plots of the real part (a) and imaginary part (b) of the observation data u with the plane incident wave when $k = 1$ and no noise in Example 1.

First, we employ the plane incident wave with the NtD map, namely injecting the Neumann input data to generate the potential u. Figure 1 shows the contour plots of the real and imaginary parts, respectively, of the near-field potential data u when $k = 1$. Except very few clues like self-similar patterns and periodicity, it is very hard to envisage the shape of the obstacle. The inverse problem we are confronted with is to reconstruct the obstacle D from those elusive plots.

We show the contour plot of the g-norm of the indicator function in Figure 2(a) and the buried unit disk can be approximately reconstructed with the cut-off value V_{cut} chosen to be -0.388 as shown in Figure 2(b). For the res-norm case, the contour plot and the identified object with the cut-off value V_{cut} chosen to be -1.98 are shown in in Figure 2(c) and (d), respectively. It is emphasized that the identified object should be understood as the union of two identified objects specified by the g-norm and res-norm. More precisely, the interior region of the object, according to Theorems 2.5 and 3.3, consists of two parts : those points with g-norm smaller than the first cut-off value, or those with res-norm smaller than the second cut-off value. It is very interesting that both indicators, g-norm and res-norm, yield nearly similar reconstructed objects independently. This phenomena remains not only for this example, but also for the rests in the sequel. By taking the set union, we may complement the identified preliminary results from the respective g-norm and res-norm with each other to synthesize a better final reconstructed object using postprocessing techniques from imaging processing, which will be further investigated and reported elsewhere. For the current stage, we will still focus on the effectiveness of the proposed reconstruction scheme.

The unknown object can be soundly detected with correct location and approximate shape and size. The blow-up behavior of the g-norm, predicted by our theoretical result, is clearly shown in Figure 2(a) . The res-norm indicator function also reveals a pattern of blow-up. With suitable choice of the threshold value V_{cut}, the res-norm at

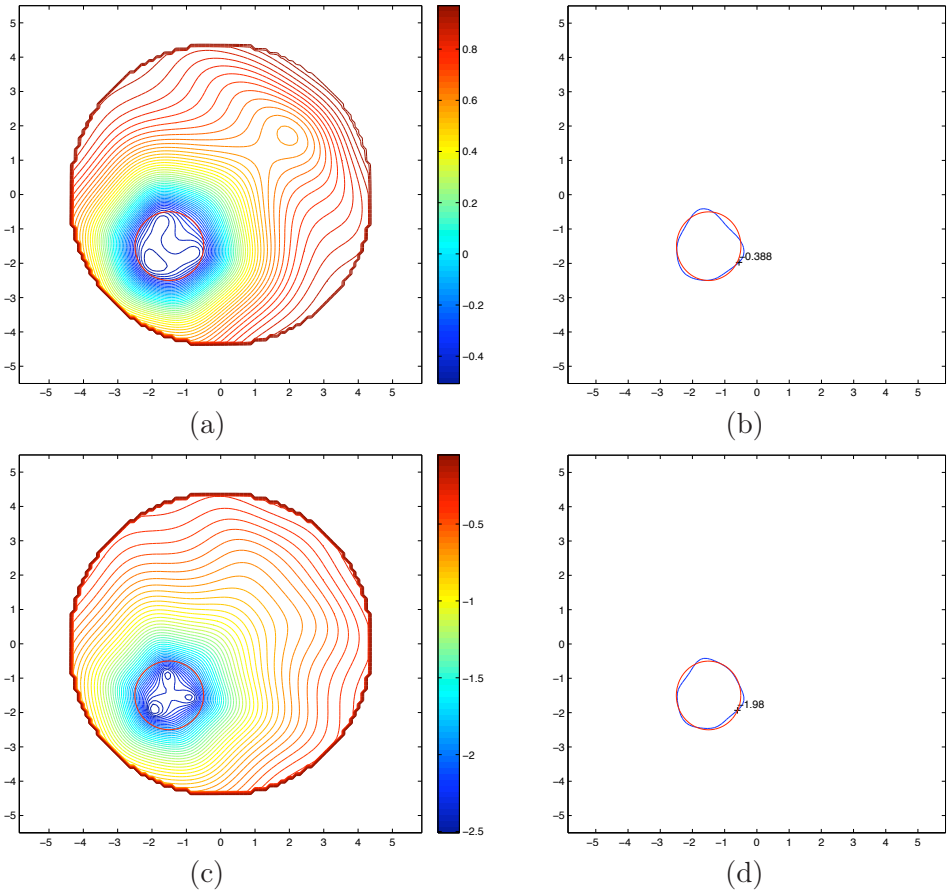

Figure 2: Example 1 with the plane incident wave when $k = 1$, the NtD map, and $\delta = 1\%$. Contour plots of the g-norm indicator (a) and res-norm indicator (c). Reconstructed obstacles from the g-norm (b) and res-norm (d) with the reference obstacle in the red line and reconstructed one in the blue line.

sampling points outside the obstacle is always larger than V_{cut}, which further consolidate the second part of Theorem 3.3 and make a distinct difference between inverse far-field and near-field scattering problems. That is, one has two groups of indicator functions which can be both used for shape reconstruction. It is a good open question to ask whether they are equivalent and how to combine them together to make better recovery of obstacles.

It is pointed out that the choice of the cut-off value is crucial for the reconstruction. The same idea from [26] can be extended here for the determination of cut-off values for inverse near-field scattering problems by taking advantage of the mutual interaction between obstacle components. We will further demonstrate the effectiveness of such choice scheme with the multi-component obstacle case in Example 3.

Next, we keep all the previous setting the same except using the DtN map, namely enforcing the boundary potential to generate the flux data $\frac{\partial u}{\partial \nu}$. Since the DtN map

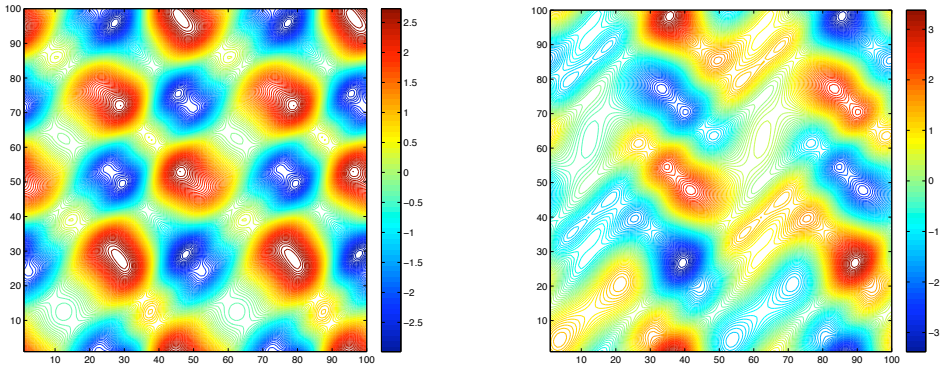

(a) (b)

Figure 3: Contour plots of the real part (a) and imaginary part (b) of the observation data $\frac{\partial u}{\partial \nu}$ with the plane incident wave when $k = 1$ and no noise in Example 1.

seems very sensitive to noise by our numerical experience, no noise is added to the measurement data in this case while there are still some inherent error due to discrete finite element solver. The contour plots of the real and imaginary parts, respectively, of the near-field flux data $\frac{\partial u}{\partial \nu}$ are shown in Figure 3.

The contour plots of the g-norm and res-norm indicator functions are presented in Figure 4(a) and (c), respectively. Then the identified obstacles can be recovered by choosing the cut-off values V_{cut} to be 0.247 and -2.94, respectively and shown in Figure 4(b) and (d), respectively. We see that the res-norm indicator gives a nearly perfect reconstruction of the disk-shape object while the identified object from the g-norm indicator is a bit compressed and deformed along the direction emanating from the origin toward the object.

Lastly, we change the incident wave from plane to cylindrical case with order $\nu = 1$ and use the NtD map while keeping all the other parameters unchanged. The contour plots of the real and imaginary parts, respectively, of the near-field potential data u are shown in Figure 5. Based on the contour plots of the g-norm and res-norm indicator functions in Figure 6(a) and (c), respectively, one can approximately recover the obstacle by choosing the cut-off values V_{cut} to be 0.993 and -2.9527, respectively, (see Figure 6(b) and (d), respectively).

***Example* 2.** Kite obstacle with $c = (0, 0)^T$.

We change the disk obstacle to be a non-convex kite-shaped obstacle in this example. First, we try the plane incident wave with the NtD map. Figure 7 shows the contour plots of the real and imaginary parts, respectively, of the near-field potential data u when $k = 1$.

From the contour plots of the g-norm and res-norm indicator functions in Figure 8(a) and (c), respectively, the obstacle can be reconstructed by choosing the cut-off values V_{cut} to be -0.286 and -1.92, respectively, as shown in Figure 8(b) and (d), respectively. We see again that the res-norm reconstruction performs better than the

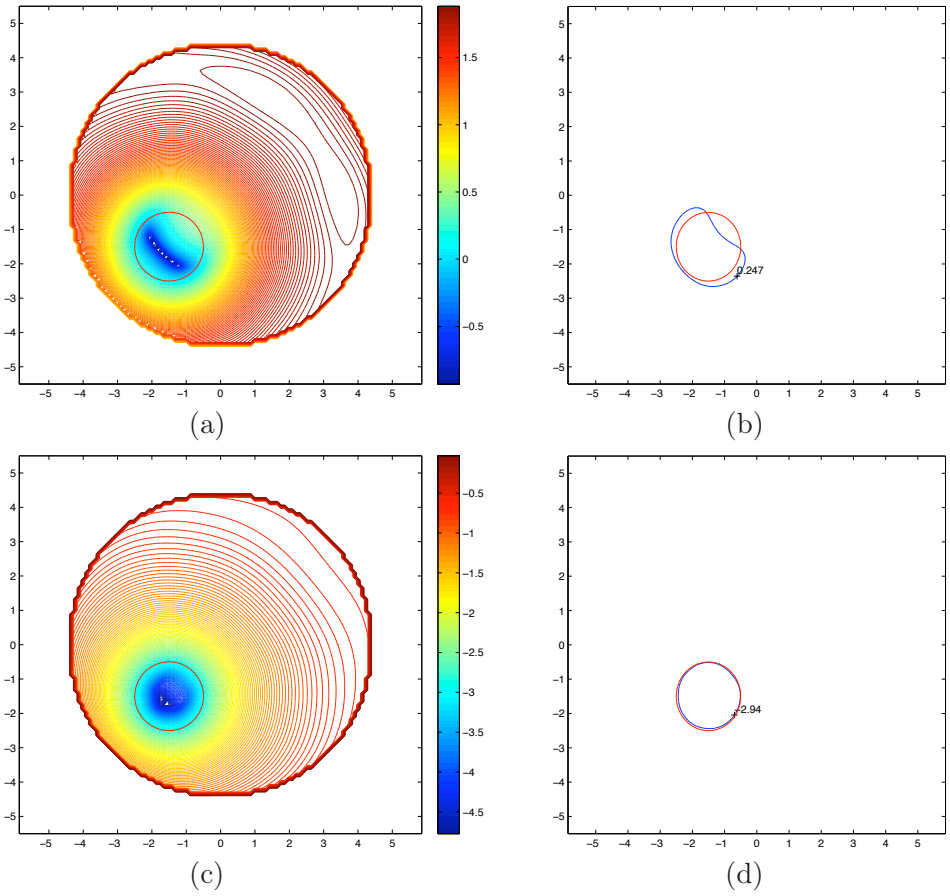

Figure 4: Example 1 with the plane incident wave when $k = 1$, the DtN map, and $\delta = 0$. Contour plots of the g-norm indicator (a) and res-norm indicator (c). Reconstructed obstacles from the g-norm (b) and res-norm (d) with the reference obstacle in the red line and reconstructed one in the blue line.

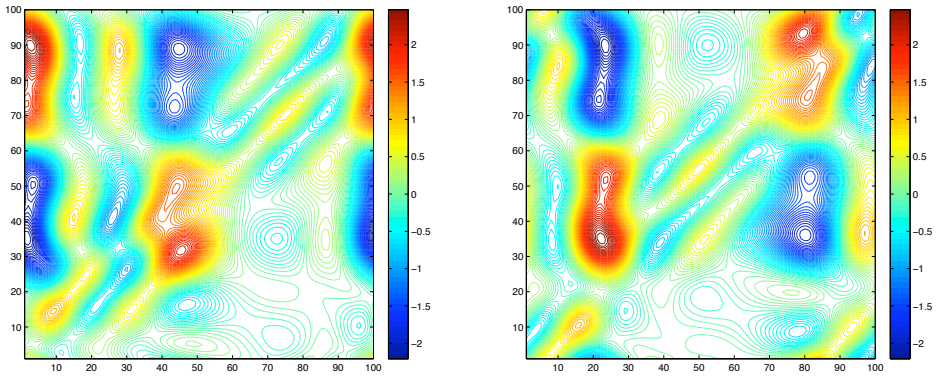

(a) (b)

Figure 5: Contour plots of the real part (a) and imaginary part (b) of the observation data u, with the cylindrical incident wave with order $\nu = 1$ and no noise in Example 1.

g-norm one, in which case the kite is slightly exaggerated to the left tip part.

Next, we repeat the test using the cylindrical incident wave of higher order $\nu = 3$ with other parameters unchanged. The contour plots of the real and imaginary parts, respectively, of the near-field potential data u when $\nu = 3$ are shown in Figure 9. It can be seen from Figure 9 that there are more patterns observed and the magnitude (around 0.8) of the measured potential u is smaller than previously due to the fast decay of the cylindrical Bessel wave as ν increases.

The reconstructed obstacles in Figure 10(c) and (d) are similar to those of the plane wave case by choosing the V_{cut} to be 0.519 and -1.91, respectively, based on the contour plots of the g-norm and res-norm indicator functions in Figure 10(a) and (c), respectively.

***Example* 3.** A combination of ball and kite obstacles with $c_{ball} = (-2, -2)$ and $c_{kite} = (2, 2)^T$.

In this example, we test the multi-component obstacle scattering case with a combination of a unit ball and a kite with some displacement. Here the plane incident wave with the NtD map is used. Figure 11 shows the contour plots of the real and imaginary parts, respectively, of the near-field potential data u when $k = 1$.

On the one hand, due to strong interaction from the close distance, those parts of different objects facing each other are attracted to a certain degree, which causes those parts looks a bit deformed. Nevertheless, the identified object is still a reasonable approximation of the original multi-component unknown obstacle. We show the contour plot of the g-norm indicator function in Figure 12(a) and the multi-component obstacle can be approximately reconstructed with the cut-off value V_{cut} chosen to be -0.255 as shown in Figure 12(b). For the res-norm case, the contour plot and the identified object with the cut-off value V_{cut} chosen to be -2.34 are shown in in Figure 12(c) and (d), respectively. In this example, the reconstruction based on the g-norm indicator seems better than that based on the res-norm, particularly for those parts facing each

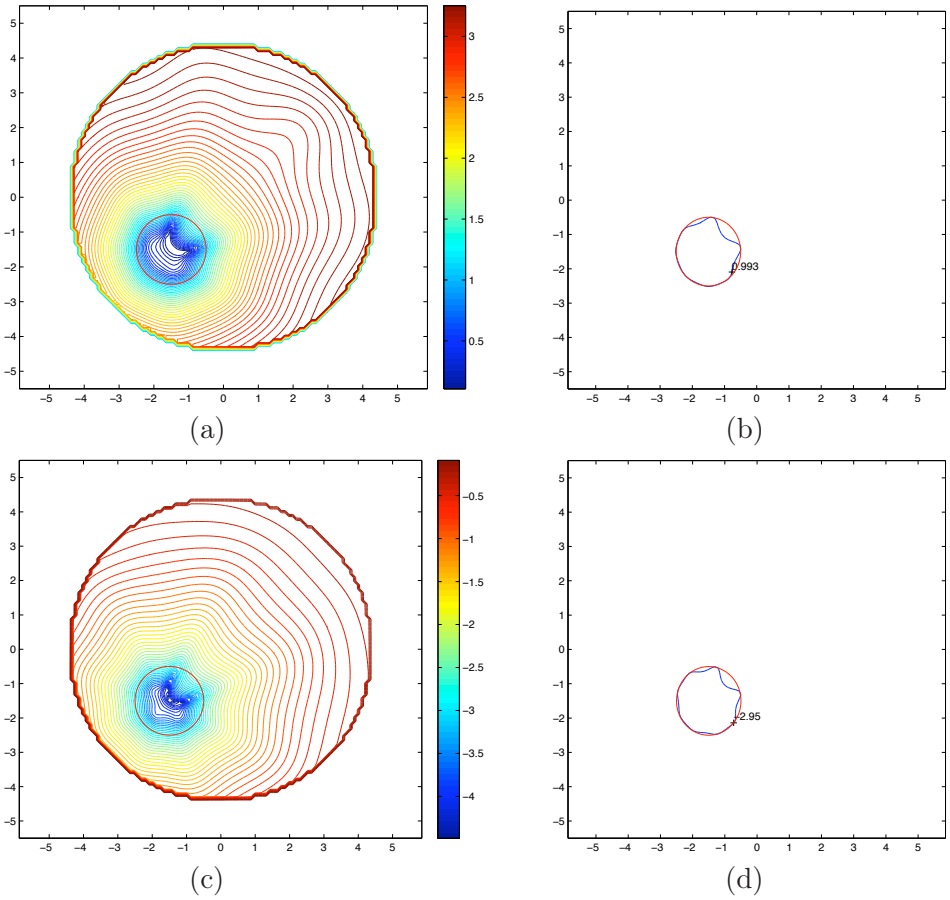

Figure 6: Example 1 with the cylindrical incident wave of order $\nu = 1$, the NtD map, and $\delta = 1\%$. Contour plots of the g-norm indicator (a) and res-norm indicator (c). Reconstructed obstacles from the g-norm (b) and res-norm (d) with the reference obstacle in the red line and reconstructed one in the blue line.

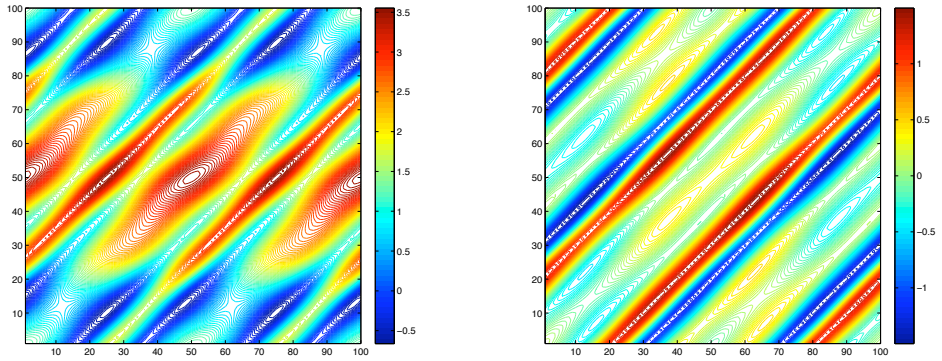

(a) (b)

Figure 7: Contour plots of the real part (a) and imaginary part (b) of the observation data u with the plane incident wave when $k = 1$ and no noise in Example 2.

other.

On the other hand, this example can be explained in an alternative way, namely it provides a similar reference idea as in [26] to choose the cut-off value in the inverse near-field obstacle scattering problems, which is in light of the mutual interaction between the components of the objects. In this example, the unit disk can be used as a reference object a priori known, we may pick out the cut-off value from the isoline which matches best the known component, and then use it to plot the isoline with the same cut-off value to recover the unknown kite component. We see clearly that the cut-off values of the two objects are correlated with each other due to the mutual interaction of wave between the objects. Furthermore, due to the interaction, those parts of objects facing each other are slightly attracted due to much stronger interaction effects with smaller distance between those parts.

6 Conclusions and future work

In this work, we develop a linear sampling type method for the inverse near-field obstacle scattering problem using the DtN or NtD maps with plane or cylindrical incident waves with resort to the blow-up phenomena of the g-norm or the lower bound of the res-norm. The method is mathematically justified along the similar line in view of the dense results of the corresponding integral operators. It is pointed out that the argument in the present paper can be further generalized to encompass the point source wave forms, which will be reported elsewhere.

References

[1] Abramowitz, M. and Stegun I. A., *Handbook of Mathematical Functions*, New York: Dover Publications, 1965

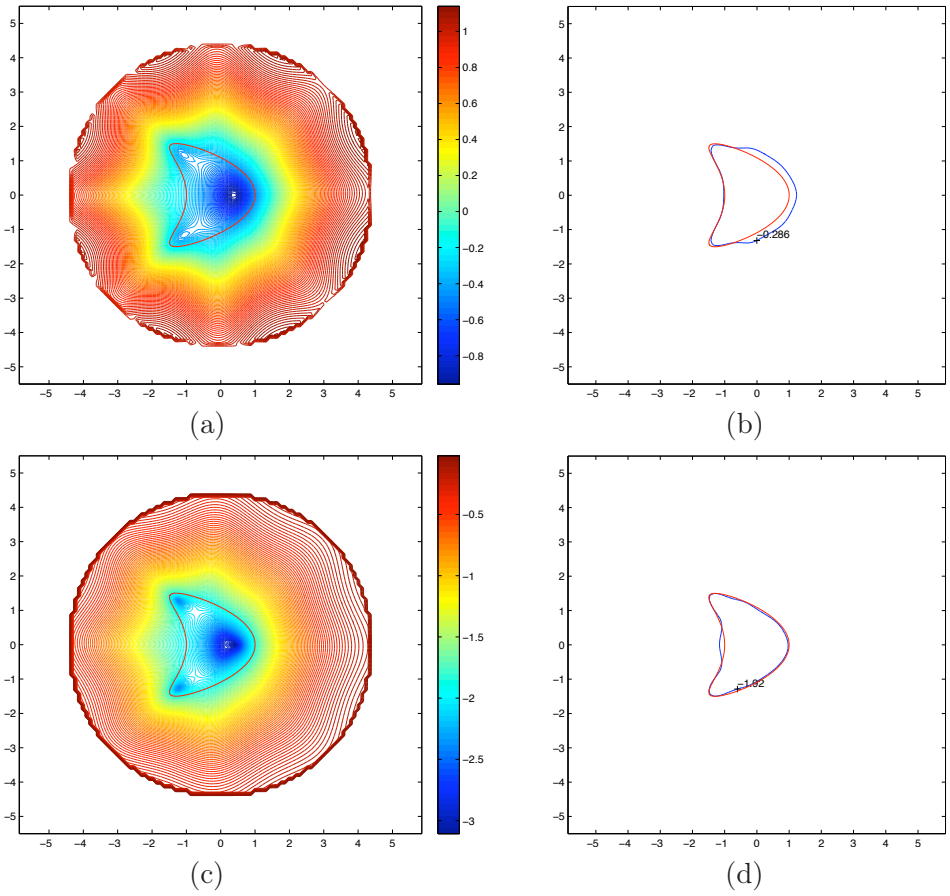

Figure 8: Example 2 with the plane incident wave when $k = 1$, the NtD map, and $\delta = 1\%$. Contour plots of the g-norm indicator (a) and res-norm indicator (c). Reconstructed obstacles from the g-norm (b) and res-norm (d) with the reference obstacle in the red line and reconstructed one in the blue line.

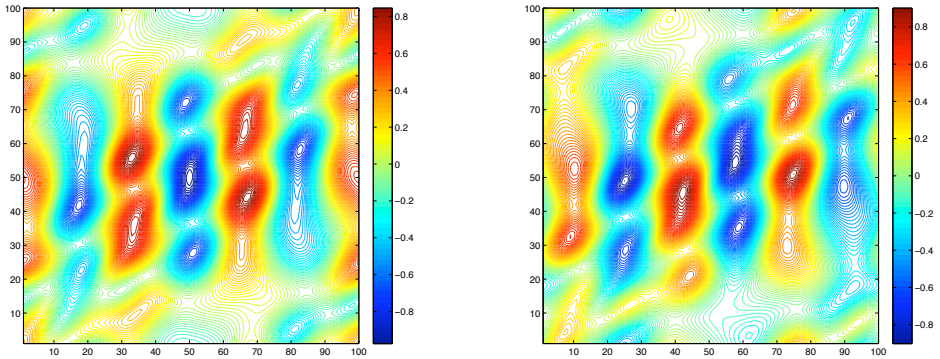

(a) (b)

Figure 9: Contour plots of the real part (a) and imaginary part (b) of the observation data u, with the cylindrical incident wave of order $\nu = 3$ and no noise in Example 2.

[2] Ammari, H., Griesmaier, R. and Hanke, M., *Identification of small inhomogeneities: Asymptotic factorization*, Math. Comp., **76** (2007), 1425–1448.

[3] Arens, T., *Why the linear sampling method works*, Inverse Problems, **20** (2004), 163–173.

[4] Cakoni, F. and Colton, D., *Qualitative Methods in Inverse Scattering Theory*, Springer, 2006.

[5] Cavicchi, T. J. and O'Brien, W. D. Jr., *Acoustic sacttering of an incident cylindrical wave by an infinite circular cylinder*, IEEE Trans Ultrason. Ferroelectr. Freq. Control, **35** (1988), 78–80.

[6] Chen, Y., *Inverse scattering via skin effect*, Inverse Problem, **13**(1997), 647–667.

[7] Cheney, M., *The linear sampling method and the MUSIC algorithm*, Inverse Problems, **17** (2001), 591-595.

[8] Chew, W. C., *Waves and Fields In Inhomogenenous Media*, Van Nostrand Reinhold, 1990.

[9] Colton, D. and Haddar, H., An application of the reciprocity gap functional to inverse scattering theory, Inverse Problems, **21** (2005), no. 1, 383–398.

[10] Colton, D., Haddar, H. and Piana, M. *The linear sampling method in inverse electromagnetic inverse scattering theory*, Inverse Problems, **19** (2003), S105-37

[11] Colton, D. and Kirsch, A., *A simple method for solving inverse scattering problems in the resonance region*, Inverse Problems, **12** (1996), 383.

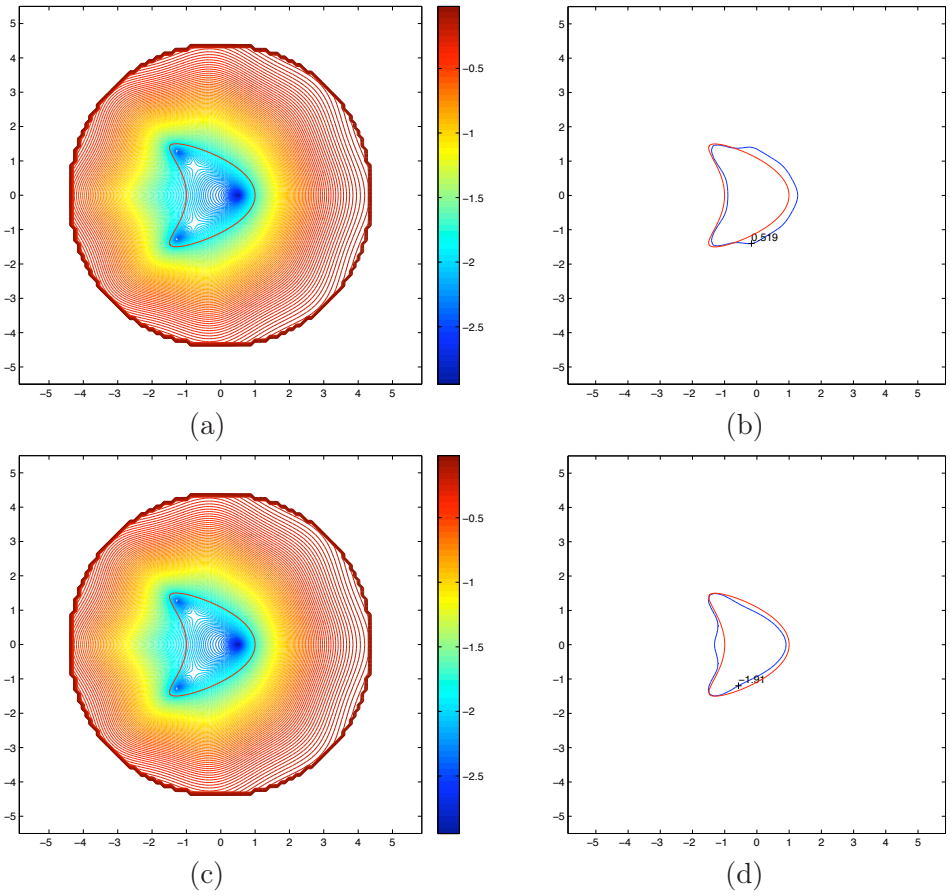

Figure 10: Example 2 with the cylindrical incident wave of order $\nu = 3$ and the NtD map with $\delta = 1\%$. Contour plots of the g-norm indicator (a) and res-norm indicator (c). Reconstructed obstacles from the g-norm (b) and res-norm (d) with the reference obstacle in the red line and reconstructed one in the blue line.

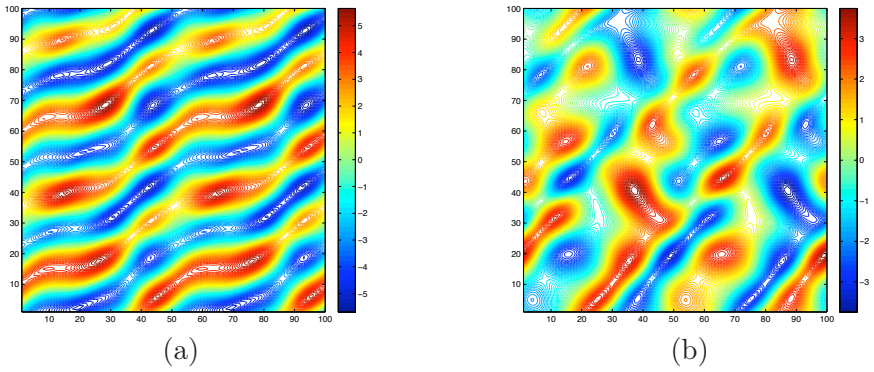

Figure 11: Contour plots of the real part (a) and imaginary part (b) of the observation data u with the plane incident wave when $k = 1$ and no noise in Example 3.

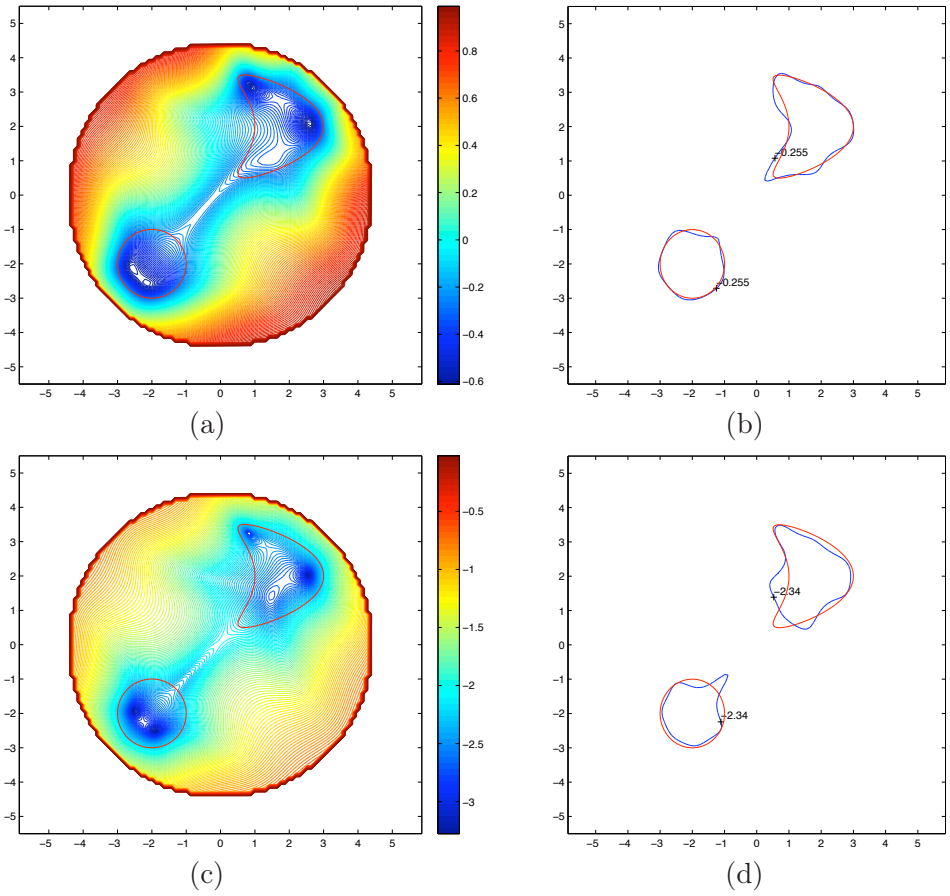

Figure 12: Example 3 with the plane incident wave and the NtD map with $k = 1$ with $\delta = 1\%$. Contour plots of the g-norm indicator (a) and res-norm indicator (c). Reconstructed obstacles from the g-norm (b) and res-norm (d) with the reference obstacle in the red line and reconstructed one in the blue line.

[12] Colton, D. and Kress, R., *Inverse Acoustic and Electromagnetic Scattering Theory*, 2nd edition, Springer-Verlag, New York, 1998.

[13] Colton, D. and Kress, R., *Using fundamental solutions in inverse scattering*, Inverse Problems, **22** (2006), R49.

[14] Colton, D. and Monk, P., *A linear sampling method for the detection of leukemia using microwaves*, SIAM J. Appl. Math., **58** (1998), 926–941.

[15] Colton, D. and Sleeman, B. D., *An approximation property of importance in inverse scattering theory*, Proceedings of the Edinburgh Mathematical Society, **44** (2001), 449–544.

[16] Dos Santos Ferreira, D., Kenig, C. E., Sjöstrand, J. and Uhlmann, G., *Determining a magnetic Schrödinger operator from partial Cauchy data*, Commu. Math. Phys., **271** (2007), 467–488.

[17] Gebauer, B., Hanke, M., Kirsch, A., Muniz, W. and Schneider, C., *A sampling method for detecting buried objects using electromagnetic scattering*, Inverse Problems, **21** (2005), 2035–2050.

[18] Gilbarg, D. and Trudinger N. S., *Elliptic Partial Differential Equations of Second Order*, Springer, 2001.

[19] Ide, T., Isozaki, H., Nakata, S., Siltanen, S. and Uhlmann, G., *Probing for electrical inclusions with complex spherical waves*, Commu. Pure. Appl. Math., **60** (2007), 1415–1442.

[20] Ikehata, M. and Itou, H., *Extracting the support function of a cavity in an isotropic elastic body from a single set of boundary data*, Inverse Problems, **25** (2009), 105005.

[21] Ikehata, M., *Enclosing a polygonal cavity in a two-dimensional bounded domain from Cauchy data*, Inverse Problems, **15** (1999), 1231–1241.

[22] Ikehata, M., *How to draw a picture of an unknown inclusion from boundary measurements. Two mathematical inversion algorithms*, J. Inv. Ill-posed Problems, **7** (1999), 255–271.

[23] Isakov, V., *Inverse Problems for Partial Differential Equations*, New York: Springer, 2n ed., 2006.

[24] Kirsch, A. and Grinberg, N., *The Factorization Method for Inverse Problems*, Oxford University Press, 2008.

[25] Li J., Liu H., and Zou J., *Multilevel linear sampling method for inverse scattering problems*, SIAM J. Sci. Comp., **30** (2009), 1228–1250.

[26] Li J., Liu H., and Zou J., *Strengthened linear sampling method with a reference ball*, SIAM J. Sci. Comp., **31** (2009), 4013–4040.

[27] Mclean, W., *Strongly Elliptic Systems and Boundary Integral Equations*. Cambridge University Press, 2000

[28] Nakamura, G. and Yoshida, K., *Identification of a non-convex obstacle for acoustical scattering*, J. Inv. Ill-posed Problems, **15** (2007), 611–624.

[29] Potthast, R., *Point Sources and Multipoles in Inverse Scattering Theorey*, Chapman& Hall/CRC Research Notes in Math., 2001.

[30] Potthast, R., *A survey on sampling and probe methods for inverse problems*, Inverse Problems, **22** (2006), R1.

Research Reports

No.	Authors/Title
10-43	*J. Li, H. Liu, H. Sun and J. Zou* Reconstructing acoustic obstacles by planar and cylindrical waves
10-42	*E. Kokiopoulou, D. Kressner and Y. Saad* Linear dimension reduction for evolutionary data
10-41	*U.S. Fjordholm* Energy conservative and -stable schemes for the two-layer shallow water equations
10-40	*R. Andreev and Ch. Schwab* Sparse tensor approximation of parametric eigenvalue problems
10-39	*R. Hiptmair, A. Moiola and I. Perugia* Stability results for the time-harmonic Maxwell equations with impedance boundary conditions
10-38	*I. Hnětynková, M. Plešinger, D.M. Sima, Z. Strakoš and S. Van Huffel* The total least squares problem in $AX \approx B$. A new classification with the relationship to the classical works
10-37	*S. Mishra* Robust finite volume schemes for simulating waves in the solar atmosphere
10-36	*C. Effenberger, D. Kressner and C. Engström* Linearization techniques for band structure calculations in absorbing photonic crystals
10-35	*R. Hiptmair and C. Jerez-Hanckes* Multiple traces boundary integral formulation for Helmholtz transmission problems
10-34	*H. Harbrecht and Ch. Schwab* Sparse tensor finite elements for elliptic multiple scale problems
10-33	*K. Grella and C. Schwab* Sparse tensor spherical harmonics approximation in radiative transfer
10-32	*P. Kauf, M. Torrilhon and M. Junk* Scale-induced closure for approximations of kinetic equations
10-31	*M. Hansen* On tensor products of quasi-Banach spaces
10-30	*P. Corti* Stable numerical scheme for the magnetic induction equation with Hall effect